coatings

Article

PVTF Nanoparticles/PLA Electroactive Degradable Membrane for Bone Tissue Regeneration

Suzhan Shi [1], Xun Xu [2], Xuzhao He [1], Siyuan Fan [1], Pengruofeng Liu [3], Chengwei Wu [1,*] and Kui Cheng [1,*]

[1] School of Materials Science and Engineering, State Key Laboratory of Silicon and Advanced Semiconductor Materials, Center of Rehabilitation Biomedical Materials, Hangzhou 310027, China; 22126059@zju.edu.cn (S.S.); hf@zju.edu.cn (X.H.); 12126073@zju.edu.cn (S.F.)
[2] Department of Stomatology, Xinjiang Second Medical College, Xinjiang 834099, China; xx1914287166@126.com
[3] The First Affiliated Hospital, School of Medicine, Zhejiang University, Hangzhou 310003, China; liupengruofeng@163.com
* Correspondence: wuchengwei@zju.edu.cn (C.W.); chengkui@zju.edu.cn (K.C.)

Abstract: Electroactive biomaterials can influence the microenvironment between cells and a material's surface by controlling surface electrical signals, thereby affecting cellular physiological activities. As the most commonly used ferroelectric polymer, Poly(vinylidene fluoride-trifluoroethylene) (PVTF) has attracted widespread attention due to its good stability, biocompatibility and mechanical properties. However, it has limitations such as non-degradability. In this study, PVTF nanoparticles (PVTF NPs), prepared using a phase separation method, were compounded with polylactide (PLA) to prepare PVTF NPs/PLA composite membrane (PN/PLA), which simultaneously achieved electroactivity and degradability. PVTF NPs containing ferroelectric β phase were evenly distributed on the PLA substrate, forming negative potential spots through corona polarization. The PLA substrate gradually degraded in a simulated body fluid environment. The negative surface potential provided by PVTF NPs in PN/PLA enhanced the adhesion, proliferation, and early-stage osteogenic differentiation of bone marrow mesenchymal stem cells (BMSCs). The electrical bioactivity and degradability could be joined together in this study, which is promising for tissue regeneration biomaterials, such as guided bone regeneration membrane.

Keywords: electroactive biomaterial; degradable material; PVTF; PLA

Citation: Shi, S.; Xu, X.; He, X.; Fan, S.; Liu, P.; Wu, C.; Cheng, K. PVTF Nanoparticles/PLA Electroactive Degradable Membrane for Bone Tissue Regeneration. *Coatings* **2024**, *14*, 115. https://doi.org/10.3390/coatings14010115

Academic Editor: Andriy Voronov

Received: 13 December 2023
Revised: 5 January 2024
Accepted: 10 January 2024
Published: 15 January 2024

1. Introduction

Electroactive biomaterials can influence the microenvironment between cells and a material's surface by controlling surface electrical signals, thereby affecting cellular physiological activities [1–4]. Electroactive biomaterials include ferroelectric, piezoelectric [5,6], electret [7,8], and conductive materials [9], among others. The electroactivity of ferroelectrics derives from bound charges of ferroelectric domains. As the centers of positive and negative charges in their lattice are misaligned, they can produce an electric dipole moment even in the absence of an applied electric field.

The application of electroactive materials in bone repair can be traced back to the discovery of the piezoelectric effect in bone in 1957 [10]. Bioelectrical signals play an important role in regulating cell growth and osteogenesis. Building a reasonable electrical microenvironment at the bone defect area through tissue engineering materials can accelerate the repair process. Under the action of electric field polarization, ferroelectric materials can maintain their surface potential for a long time, which can simulate the natural electrical signals of natural bone tissue. Polyvinylidene fluoride (PVDF) stands as one of the most prevalent organic ferroelectric materials. Acclaimed for its superior stability, biocompatibility [11,12], and mechanical performance, it is widely used in the field of bone repair.

The significant difference in electronegativity between the F and H atoms in the PVDF molecular chain forms electric dipole moments from F to H. The directional arrangement of dipole moments creates macroscopic potential [13]. PVDF has four crystal phases, of which the β-phase has a trans conformation and exhibits the largest piezoelectric properties [14]. By inserting trifluoroethylene units into the PVDF molecular structure, the crystallinity of the β-phase can be significantly enhanced; hence, various copolymer ratios of Poly(vinylidene fluoride-trifluoroethylene) (PVTF) are widely utilized [15]. Tang et al. [16] designed PVTF membranes with different surface potentials and found that surface potential can regulate the binding state of proteins and integrins, thereby affecting the level of cellular osteogenic differentiation. Zhang et al. [17,18] combined magnetic particles $CoFe_2O_4$ with PVTF, utilizing the magnetostrictive effect driven by a magnetic field to induce the piezoelectric response of PVTF, thus promoting the osteogenesis of stem cells.

Apart from membrane, PVTF can also be fabricated into other structures such as nanoparticles, nanofibers [19,20], and hydrogels [21]. For instance, Mishra et al. [22] utilized a dual-solvent phase separation technique to prepare δ-phase PVTF nanoparticles (PVTF NPs), which achieve nanoscale ferroelectricity and piezoelectricity. Fu et al. [23] synthesized PVTF NPs of around 60 nm and 250 nm in size via phase separation, managing to adjust the crystallinity and the β-γ ferroelectric phase ratio by modulating the interfacial energy between DMF and water.

Electroactive materials represented by PVTF are widely used in bone tissue regeneration. However, most electroactive materials are not biodegradable. Poor biocompatibility and the need for secondary surgical removal have restricted their application. The trend towards biodegradability is a significant one in the evolution of biomaterials [24]. Determining how to combine electroactivity with biodegradability is a challenge. Natural materials and biodegradable polymers are two common approaches. Bio-based materials, such as bones [25], collagen [26], and various protein-based materials, exhibit piezoelectric characteristics. However, the piezoelectric performance of these natural materials is relatively weak, so various strategies need to be employed to enhance their macroscopic piezoelectricity [27,28]. Another approach involves biodegradable polymers.

Polylactide (PLA) is a polymer with good biodegradability, biocompatibility, and suitable mechanical properties. PLA can be degraded by simple hydrolysis of ester bonds in aqueous environments such as body fluids, and the degradation products are carbon dioxide and water that the human body can metabolize. PLA has been widely used in tissue engineering scaffolding materials [29], absorbable surgical sutures, controlled-release drug carriers, etc. In addition to degradability, PLA exhibits shear piezoelectricity [30–32], which is due to the displacement of C=O bonds when subjected to shear stress, thus engendering net dipole moments and electrical charges. Researchers fabricated PLA nanofiber networks via electrospinning and found that dipoles undergo favorable orientation under tensile and polarizing conditions [33]. Moreover, the shear piezoelectric properties of PLA nanowires were discerned using piezoresponse force microscopy [34].

In this study, a PVTF NPs/PLA (PN/PLA) composite membrane was prepared by combing ferroelectric PVTF NPs with PLA to integrate electroactivity and biodegradability. This study investigated the ferroelectricity of PVTF NPs, the surface potential of the composite membrane, and its degradation. The impact of polarization and PVTF NPs on biocompatibility and the promotion of bone differentiation was also studied. This research presents a strategy for integrating electroactivity and biodegradability, paving new pathways for the development of high-performance biomaterials.

2. Materials and Methods

2.1. Preparation of PVTF NPs

P(VDF-TrFE) (Piezotech, Paris, French, VDF:TrFE = 70:30) was dissolved in DMF (Aladdin Chemical Reagent, Shanghai, China) to form Solution A at a concentration of 15 mg/mL, while deionized water served as Solution B. After that, 2 mL DMF was added to a test tube as a buffer layer. Next, 10 mL Solution A was slowly introduced on top of the DMF, and 10 mL Solution B was slowly injected beneath the DMF layer, then it was left to stand at 25 °C for 120 min to produce a stable stratification. The lower layer was collected and centrifuged to obtain PVTF NPs precipitates. Anhydrous ethanol was added to the PVTF NPs precipitates, and the mixture was thoroughly vortexed and sonicated to uniformly disperse the PVTF NPs into anhydrous ethanol.

2.2. Preparation of PN/PLA Membrane

PLA (Huanuo Biomaterials, Changchun, China, molecular weight 200,000) was dissolved in 1,4-dioxane, coated onto a flat glass plate to form a membrane, dried at 37 °C, and cut into 1 cm × 1 cm. The PVTF NPs ethanol dispersion was spin-coated onto the PLA membranes to obtain the PN/PLA membranes. The spin coating speed was 5000 r/min and the spin coating time was 15 s. Then, PN/PLA membranes were heated at 160 °C for 30 s and allowed to cool naturally. PN/PLA was subjected to corona polarization under 10 kV for 30 min.

2.3. Characterization of Mateials

The surface morphology of nanoparticles and membranes was characterized by scanning electron microscopy (FE-SEM, Hitachi SU-70, Tokyo, Japan). The crystal phase structure was analyzed using an X-ray diffractometer (PANalytical X'Pert PRO, Almelo, The Netherlands) equipped with a Cu Kα radiation source at 30 kV and the scan rate was 2°/min for the range of 5–50°. The FTIR spectrum was analyzed via infrared spectrometer (Nicolet 5700, Thermo Fisher Scientific, Waltham, MA, USA) at a range of 500~2000 cm^{-1} using an attenuation total reflection (ATR) mode. The surface topology and roughness of the membranes were characterized by atomic force microscopy (NTEGRA Spectra, NT-MDT, Moscow, Russia). The ferroelectric properties of PVTF NPs were characterized using piezoresponse force microscopy (PFM)(NTEGRA Spectra, NT-MDT, Moscow, Russia), where a bias voltage ranging from −10 V to 10 V was applied at the tip. Surface potential measurements were conducted using scanning Kelvin probe microscopy (SKPM) (NTEGRA Spectra, NT-MDT, Moscow, Russia). Zeta potential was analyzed using a Solid Surface Zeta Potential Tester (Anton Paar surpass, Graz, Austria) at pH = 7.4.

2.4. Cell Vitality Assays and ALP Assays

Bone marrow mesenchymal stem cells (BMSCs) were isolated from 3-week-old male Sprague Dawley rats. The cells were plated onto the membrane's surface at a seeding density of 50,000 cells/cm^2 and cultured in low-glucose Dulbecco's Modified Eagle Medium (DMEM, Cellmax, Beijing, China) supplemented with 10% fetal calf serum. At 1 and 3 days post-seeding, a CCK-8 solution (Dojindo Laboratories, Kumamoto, Japan) was added to the sample at a 1:10 concentration ratio. After 2 h of incubation, a microplate reader (Multiskan MK3, Thermo Fisher Scientific, Shanghai, China) was used to measure the optical density (OD) of the solution at 450 nm.

For morphological assessment, BMSCs were seeded at a density of 5000 cells/cm^2 on the membranes. After three days, the cells were stained with DAPI (Sigma, Ronkonkoma, NY, USA) for nuclei and Alexa Fluor 594 phalloidin (ATT Bioquest, Pleasanton, CA, USA) for F-actin. The stained cells were then observed under a laser scanning confocal microscope (CLSM, ZEISS LSM780, Oberkochen, Germany).

The early osteogenic differentiation of the BMSCs was quantified by alkaline phosphatase (ALP) activity. BMSCs were seeded at 50,000 cells/cm^2 and, from the third day onwards, cultured with osteogenic induction factors (10 mM ascorbic acid, 1 mM dexamethasone, and 1 mM β-glycerophosphate sodium). After 7 and 14 days, the cell lysates were analyzed using the LabAssay ALP kit (Wako, Japan) and BCA protein assay kits (Thermo Fisher Scientific, Waltham, MA, USA).

3. Results

3.1. Preparation Principle and Morphology of Materials

PVTF NPs were prepared via a phase separation method [22,35] (Figure 1a). PVTF molecular chains and water molecules diffused at the phase boundary. Due to the hydrophobic interaction between water molecules and the -CF_2- in PVTF, the diffusion of PVTF molecular chains into the aqueous phase will disrupt the hydrogen bond network among water molecules. To compensate for the disrupted hydrogen bonds, water molecules formed additional bonds with adjacent ones, creating "ice-like cage hydrates" [36], which enveloped the PVTF molecular chains in a hydrogen bond network. The PVTF molecular chains tended to reduce their surface area in the aqueous phase, thus folding into nanoparticles. Then, nanoparticles formed at the phase interface and settled into the lower aqueous layer under gravity.

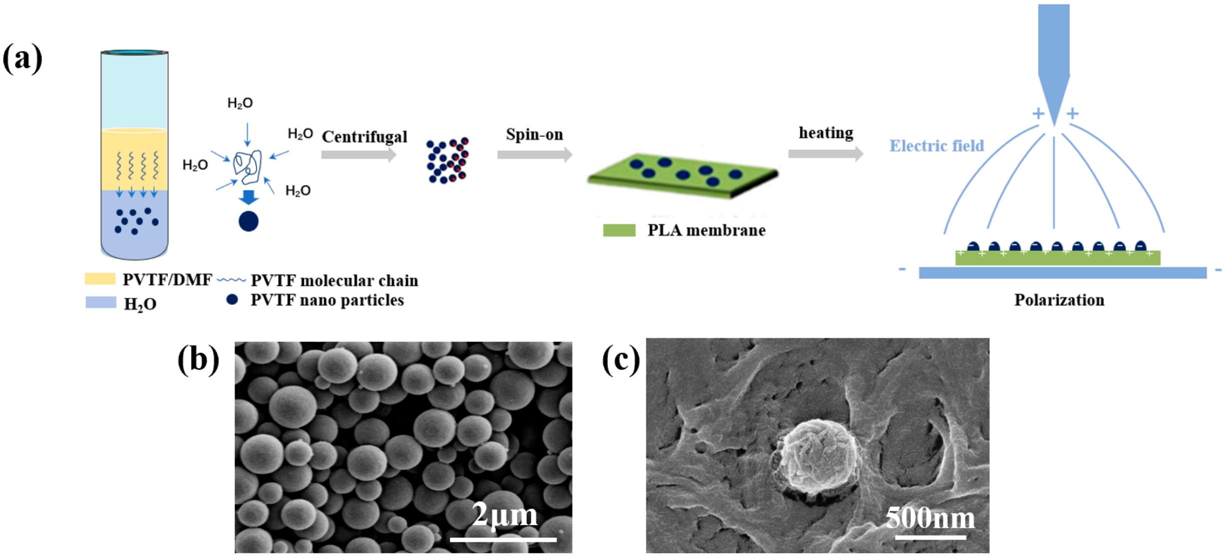

Figure 1. Preparation process of PN/PLA (**a**) and SEM images of PVTF NPs (**b**) and PN/PLA (**c**).

PVTF NPs were standard spherical shapes with smooth surfaces. The diameters of PVTF NPs were distributed between 200 and 800 nm, most of which were around 500 nm (Figure 1b).

In order to allow the PVTF NPs to function on the membrane surface and minimize the amount of non-degradable PVTF NPs, the PVTF NPs were spin-coated onto the surface of the PLA substrate and fixed by heating. The thermal treatment was performed at 160 °C, a temperature slightly above the melting point of PVTF (150.2 °C) and within the processing temperature range of PLA (148.2–187.4 °C). PVTF NPs melted during heating and crystallized during the cooling process. This resulted in striated crystallization on the surface of the PVTF NPs (Figure 1c), consistent with the characteristics of fibrillar striation in PVTF membranes after annealing [16]. Simultaneously, the bottom of the PVTF NPs melted and integrated with the PLA substrate. If the heating temperature was set to be above 160 °C, the PVTF NPs completely melted on the PLA substrate, forming blotchy crystalline patterns and losing their spherical shape. In subsequent experiments, the bond between the PVTF NPs and PLA was tight, with no evident detachment of PVTF NPs from the PLA substrate.

PN/PLA composite membrane was subjected to corona polarization. When a strong electric field was applied between the needle-tip electrode and the grounded metal plate where the sample was placed, the gas molecules near the polarizing electrode tip ionized, producing ions with the same polarity as the electrode. Under the electric field, these ions gathered on the surface of the membrane at the grounded electrode, creating an internal electric field within the membrane [37,38], which induced the alignment of PVTF dipoles.

3.2. Composition and Ferroelectricity

PVTF has four crystal forms: α, β, γ, and δ [13], among which the β-phase exhibits the strongest polarity due to its all-trans TTTT arrangement. As indicated by XRD (Figure 2a), β-phase diffraction peak of PVTF NPs was observed at 2θ = 19.8°, corresponding to the (110) and (200) crystal faces [39]. In the XRD patterns of PLA and PN/PLA, the characteristic peaks of PLA were observed at 2θ = 14.7°, 16.6°, 19.0° and 22.3°. To further obtain molecular structural information of PVTF NPs, FTIR testing was performed (Figure 2b), revealing two distinct piezoelectric phase absorption bands. The absorption peaks at 848 cm^{-1} corresponded to the symmetric stretching vibrations of CF_2 and the peak at 1402 cm^{-1} was a mixed peak of the β and γ phases, corresponding to the non-planar rocking vibration of CH_2. Compared with PLA, PN/PLA showed characteristic peaks of PVTF NPs at 848 cm^{-1} and 1402 cm^{-1}. The XRD and FTIR spectra confirmed that the β-phase was the dominant crystal formed in PVTF NPs, laying the foundation for the manifestation of macroscopic ferroelectricity. PN/PLA contains the characteristic peaks of PLA and PVTF NPs, indicating that the spin coating–heating method successfully combined PLA and PVTF NPs.

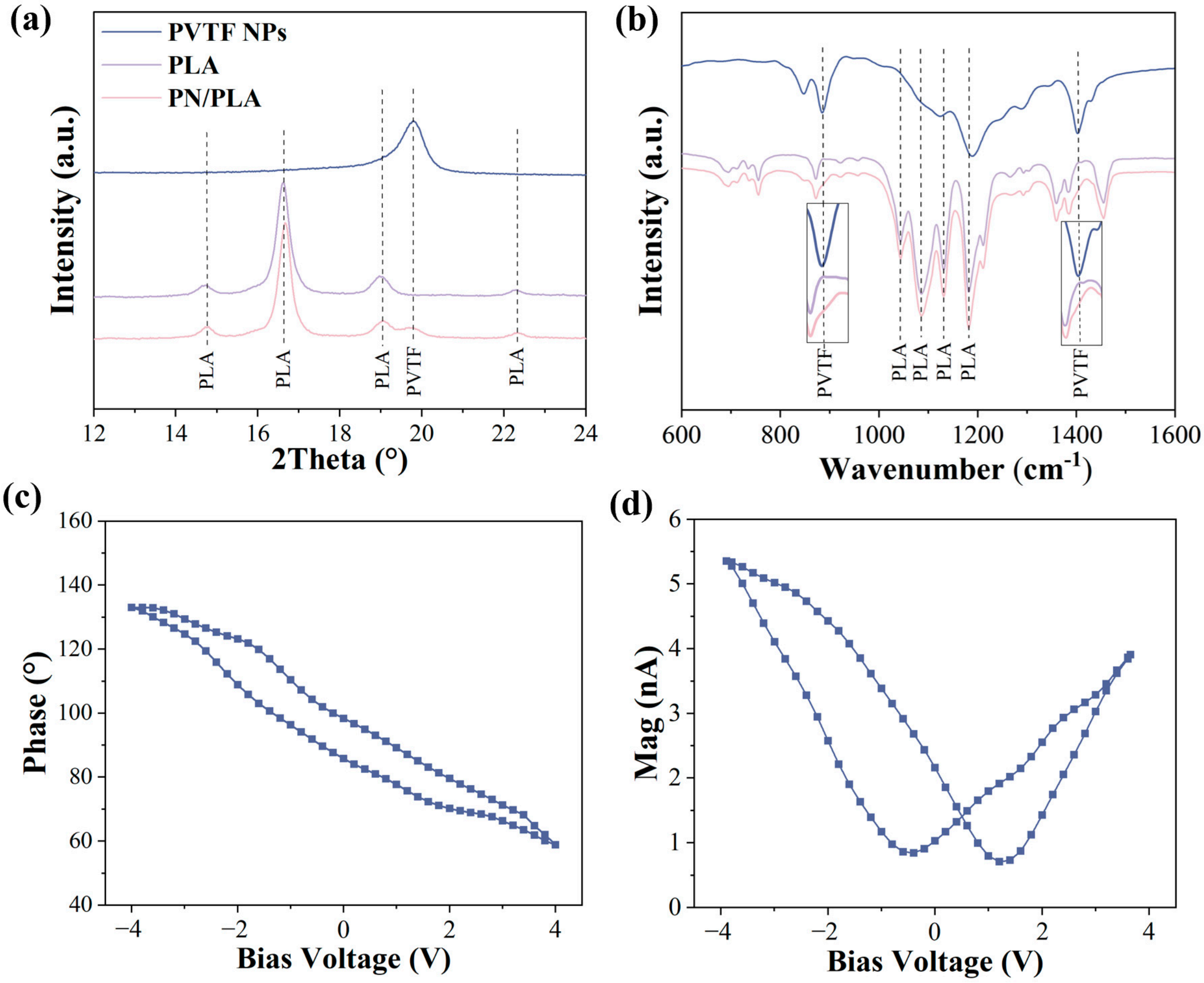

Figure 2. XRD pattern (**a**) and FTIR spectrum (**b**) of PVTF NPs, PLA and PN/PLA. Hysteresis loop (**c**) and butterfly curve (**d**) of PVTF NPs.

Atomic force microscopy was employed to measure the polarization behavior of single-PVTF NP. In KPFM mode, a voltage $V_{tip} = V_{DC} + V_{AC}$ was applied to the probe tip. V_{DC} was set between −10~10 V to create a polarization electric field within the probe's range, flipping the dipoles of the sample. $V_{AC} = V_0 \cos(\omega t)$ induced vibration in the sample due to the reverse piezoelectric effect. V_{AC} was used to detect the vibration signals, which represent the polarization intensity of the domains. PVTF NPs were placed on a silicon substrate, and V_{tip} was applied at a fixed point on the probe tip. As shown in Figure 2c, when V_{DC} increased from −4 V to 4 V, there was a 75° phase shift, indicating that the dipoles of the PVTF NPs adjusted their direction in the electric field until saturation at V_{DC} = 4 V. When a reverse voltage of 4 V to −4 V was applied, the dipoles reversed, achieving saturated polarization strength at V_{DC} = −4 V. The phase change of PVTF NPs with probe tip voltage was nonlinear and showed hysteresis, forming a hysteresis loop in the ferroelectric hysteresis curve.

Similarly, as shown in Figure 2d, when a bias of −4 to 4 V was applied, the polarization strength of the sample dropped to its lowest at 1.2 V and then reached saturation at 4 V with the increase in electric field strength. This indicated that when the direction of the electric field was opposite to the intrinsic polarization direction of the domains, the net dipole moment gradually decreased with the increasing electric field, eventually generating a reverse dipole moment. The polarization strength lagged behind the electric field strength, forming a butterfly curve. The hysteresis loop and butterfly curve demonstrated the ferroelectricity of PVTF NPs.

3.3. Surface Morpholigy and Potential of PN/PLA

Samples without corona polarization were labeled as Unpoled and those undergoing corona polarization were labeled as Poled. Four groups were established: PLA-Unpoled, PLA-Poled, PN/PLA-Unpoled and PN/PLA-Poled. The surface morphology of PLA and PN/PLA is shown in Figure 3a. PLA is a semi-crystalline polymer. After heat treatment, its surface was smooth with uniformly distributed striated crystalline patterns. There was no obvious difference in surface morphology before and after polarization. In PN/PLA-Unpoled and Poled, PVTF NPs maintained their independent spherical structures, which were evenly distributed on the PLA surface. After heat treatment, the bottom of the PVTF NPs and the PLA substrate melted and combined.

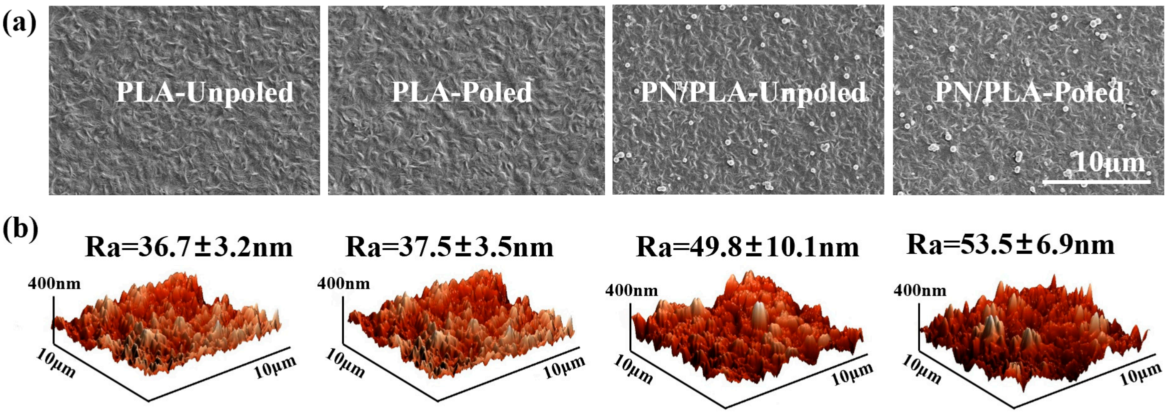

Figure 3. SEM images (**a**) and AFM scanning (**b**) of PLA and PN/PLA.

Atomic force microscopy was employed to characterize the membrane's topographic morphology and surface roughness (Figure 3b). The surface roughness (Ra) of PLA-Unpoled, PLA-Poled, PN/PLA-Unpoled and PN/PLA-Poled was, respectively, 36.7 ± 3.2 nm, 37.5 ± 3.5 nm, 49.8 ± 10.1 nm and 53.5 ± 6.9 nm. The roughness of the membranes before and after polarization showed no significant difference, indicating that corona polarization did not alter the surface roughness. PVTF NPs were distributed on the PLA surface, forming high protrusions in the 3D morphology; hence, the roughness of PN/PLA was higher than that of PLA.

The surface potentials of PLA and PVTF NP were measured by KPFM, as shown in Figure 4a. During scanning, the tip and the sample do not make direct contact, creating a capacitor-like structure. There is a work function difference between the tip and sample, so when moving the tip to change the distance between "capacitor", there is electron flow (i.e., current) in the circuit between the sample and the tip. If voltage compensation is applied to the tip, and this compensation exactly matches the work function difference between the tip and sample, the circuit's current will be zero. Therefore, when the current between the tip and sample is zero, the surface potential of the sample can be determined from the applied compensating voltage and the known work function of the tip [40,41].

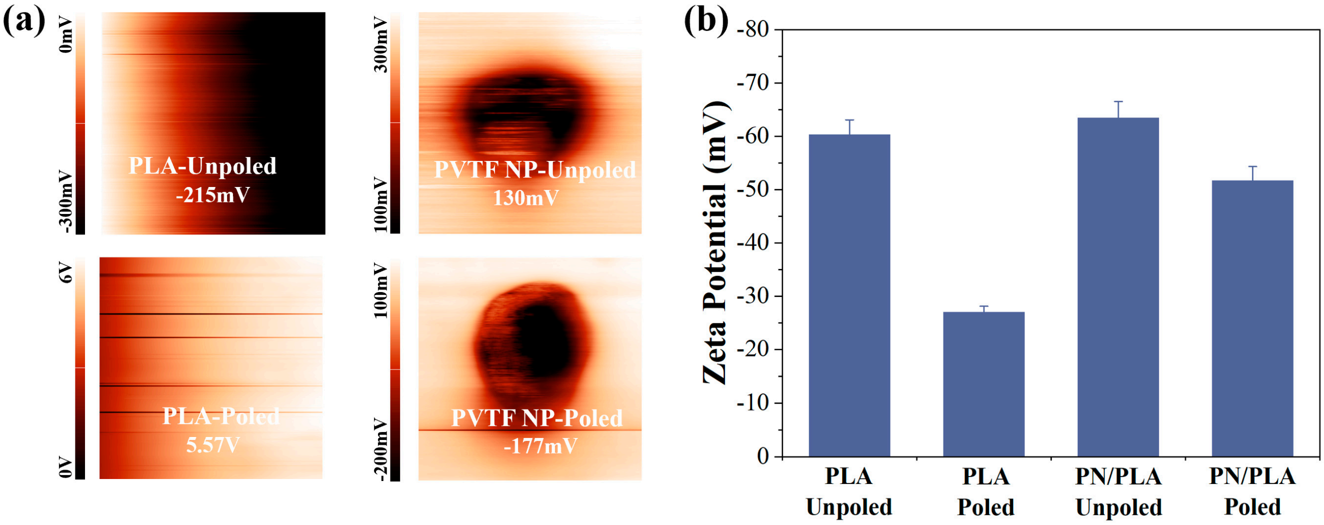

Figure 4. Surface potential of PLA and PVTF NP (**a**) and zeta potential of PLA and PN/PLA before and after polarization (**b**).

The surface potentials of PLA-Unpoled and PLA-Poled were −215 mV and 5.57 V, respectively. After corona polarization, the polarity of PLA's surface potential significantly changed. The surface potential of a single PVTF NP was 130 mV before polarization and −177 mV after polarization. PLA and PVTF NP exhibited completely opposite potential changes after polarization. During corona polarization, the positively charged tip ionizes positive ions in the air, which then concentrate on the membrane surface under the influence of an electric field. Two phenomena occur: 1. Surface ions interacting with and being injected into the polymer are fixed or trapped by the polymer. 2. A strong electric field is formed between the surface ions and the metal plate beneath the sample, aligning the dipoles within the polymer [42]. For PLA, the former effect may be stronger than the latter, with the injection of charge leading to a significant increase in surface potential to 5.57 V. This was much higher than the potential level generated by typical dipole alignment. For PVTF NP, a strong ferroelectric material, the latter effect may be stronger. Under the electric field, PVTF NP's dipoles align, causing negatively charged fluorine atoms to migrate towards the upper surface, thereby generating a potential opposite to the electric field [16].

The surface potentials in a wet state were characterized by the zeta potentials at pH = 7.4. As shown in Figure 4b, the zeta potentials of PLA-Unpoled, PLA-Poled, PN/PLA-Unpoled and PN/PLA-Poled were −60.3 mV, −27.0 mV, −63.4 mV and −51.7 mV, respectively. Firstly, the difference in surface zeta potentials between PLA-Unpoled and PN/PLA-Unpoled was minor, indicating that the surface potential of PVTF NPs before polarization was negligible. Secondly, after polarization, the surface potentials of both PLA and PN/PLA shifted in the positive direction, consistent with the trend observed in KPFM, which may be attributed to the positive shift in PLA's potential. Lastly, the zeta potential of PN/PLA-Poled was more negative than PLA-Poled and the potential shift of PN/PLA-Poled after polarization (+11.7 mV) was lower than that of PLA-Poled (+33.3 mV). It is speculated that the negative shift in PVTF NPs' potential counteracted part of PLA's positive potential shift. Therefore, PVTF NPs possibly formed potential low points and evenly distributed on the PLA substrate surface.

3.4. Degradability of PN/PLA

PN/PLA was immersed in simulated body fluid (SBF, 37 °C) for 4 weeks to observe its degradation. As shown in Figure 5a, the surface morphology of PN/PLA underwent significant changes. On the surface of PLA, fine pores began to appear and expanded between the crystalline stripes. After four weeks of immersion, a net full of pores formed, constituted by stripe-like crystalline frameworks. The surface of PVTF NPs remained stable, maintaining their individual spherical shapes with no pores or cracks on the surface. The bond between PVTF NPs and the PLA substrate remained tight over the four weeks, with essentially no detachment observed. In an ideal scenario, in the early stages of implantation, PVTF NPs bond to PLA substrate tightly and exhibit electroactivity. In the later stages, as PLA gradually degrades, PVTF NPs detach from the PLA surface, becoming free nanoparticles, and are excreted from the body with the metabolism of body fluids.

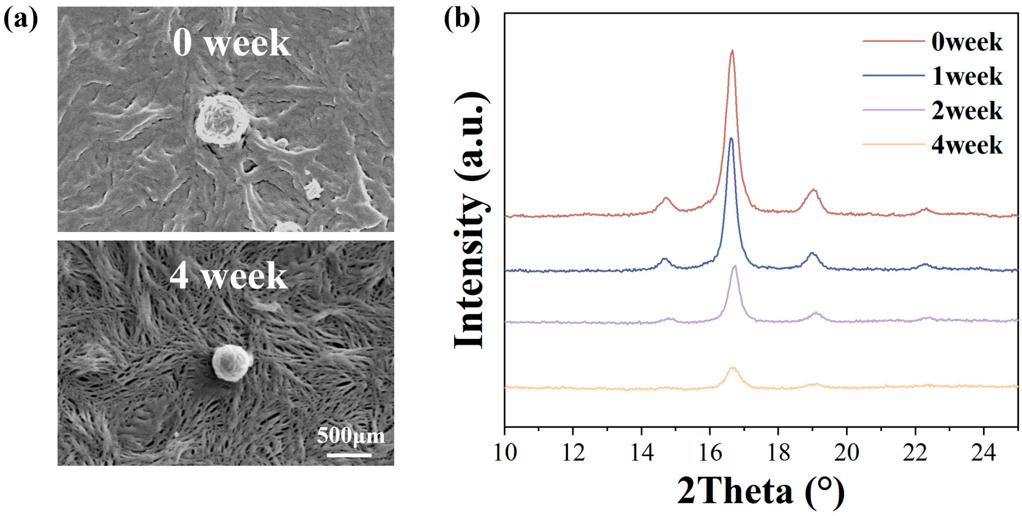

Figure 5. SEM images (**a**) and XRD patterns (**b**) of PN/PLA over a 4-week period.

The crystallinity of PN/PLA over 4 weeks of degradation was characterized by XRD (Figure 5b). At $2\theta = 14.7°$, 16.6°, and 19.0°, PLA exhibited its characteristic diffraction peaks, showing typical crystalline polymer features. During the process of degradation, the intensity of PLA characteristic peaks noticeably decreased, indicating a reduction in crystallinity.

In a simulated body fluid environment, PLA underwent uneven hydrolytic degradation. The ester groups on the molecular chains reacted with water, leading to the breakage of PLA molecular chains, gradually disordering the neatly arranged molecular chains. PLA transitioned from a crystalline state to an amorphous state, resulting in decreased crystallinity [43]. The degradation rate of PLA is related to its crystallinity. Amorphous regions degrade first, while crystalline parts degrade gradually from the outside in [44,45]. The pores resulting from the degradation of amorphous regions in Figure 4a created a network structure made of stripes.

3.5. Biocompatibility and Osteogenesis of PN/PLA

To assess the biocompatibility of the membranes, BMSCs were seeded and cultured on the surface of membranes. CCK-8 assays were conducted on the first and third days to evaluate cell adhesion and proliferation, and the results are shown in Figure 6a. The *y*-axis in the figure represents the absorbance of CCK-8, where higher absorbance indicates a higher cell count. The OD value of the first day evaluates the number of cells adhering to the membrane, and the value obtained on the third day is used to assess cell proliferation.

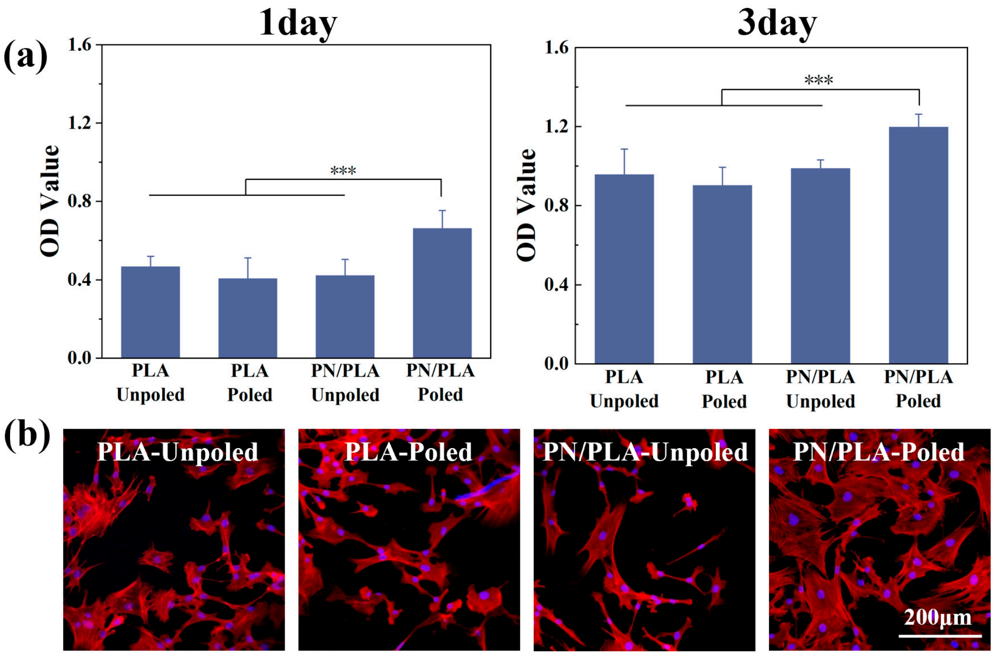

Figure 6. Adhesion, proliferation (**a**) and morphology (**b**) of BMSCs seeded on PLA and PN/PLA (*** $p < 0.001$).

After 1 and 3 days, there was no significant difference in cell numbers between PLA-Unpoled and PLA-Poled, indicating that the potential changes in PLA after corona polarization have limited effect on cell behaviors. Moreover, the cell counts on PLA-Unpoled and PN/PLA-Unpoled were comparable, so the influence of the morphology and composition of PVTF NPs can be eliminated. The cell number on PN/PLA-Poled was significantly higher than that of the other three groups, indicating that polarized PVTF NPs can promote cell adhesion and proliferation.

After culturing BMSCs on the membrane surface for 3 days, the cell morphology was observed, as shown in Figure 6b. Cells on the surface of PLA-Unpoled, PLA-Poled and PN/PLA-Unpoled appeared elongated. However, the cells on PN/PLA-Poled were in good condition, with significantly increased spreading area and perimeter. This result was consistent with the result of CCK-8 assay, indicating a significant improvement in the biocompatibility of PN/PLA-Poled, which is attributed to the surface PVTF NPs.

ALP activity, a marker of early osteogenic differentiation, was used to assess the osteogenic response of BMSCs (Figure 7). After seven days of culture, there was no notable difference in ALP activity among PLA-Unpoled, PLA-Poled and PN/PLA-Unpoled. PN/PLA-Poled achieved the highest ALP activity, which was 39.52% and 36.96% higher than PLA-Poled and PN/PLA-Unpoled, respectively. The results from 14 days were consistent with the trend observed on the seventh day.

The above results indicated that the morphology and composition of PVTF NPs, as well as the potential shift in PLA after polarization, had no significant effect on promoting osteogenic differentiation of BMSCs. PVTF NPs after polarization significantly enhance the early osteogenic differentiation of BMSCs.

PVTF NPs formed dispersed spots with negative potentials on the PLA substrate. It is speculated that such negative potentials regulate the distribution of integrins on the material surface, thereby regulating cell fate. The mechanism of PVTF NPs promoting osteogenic differentiation requires further exploration. There are several mechanisms that explain this phenomenon. Cells attach to material surfaces mainly by recognizing proteins on biological surfaces and establishing binding through integrins and proteins. The surface potential of PVTF affects the protein configuration, thereby affecting the integrin-mediated osteogenic differentiation signaling pathway. Tang et al. [16] found that on the surface of different potentials, the exposure degree and relative distance between the two main adhesion sites RGD and PHSRN between integrin α5β1 and ankyrin FN changed. Under an appropriate surface potential, integrin α5β1 and ankyrin FN can be fully bound to enhance the activation of the osteogenic differentiation pathway. Patterned material surfaces with electrical potential gradients also have an impact on osteogenic differentiation. Zhang et al. [17,18] found that locally distributed electrical signals caused local differences in integrin expression and distribution. The skeleton state of cells on the surface of the material is regulated by integrins, thereby enhancing the osteogenic differentiation ability of the cells.

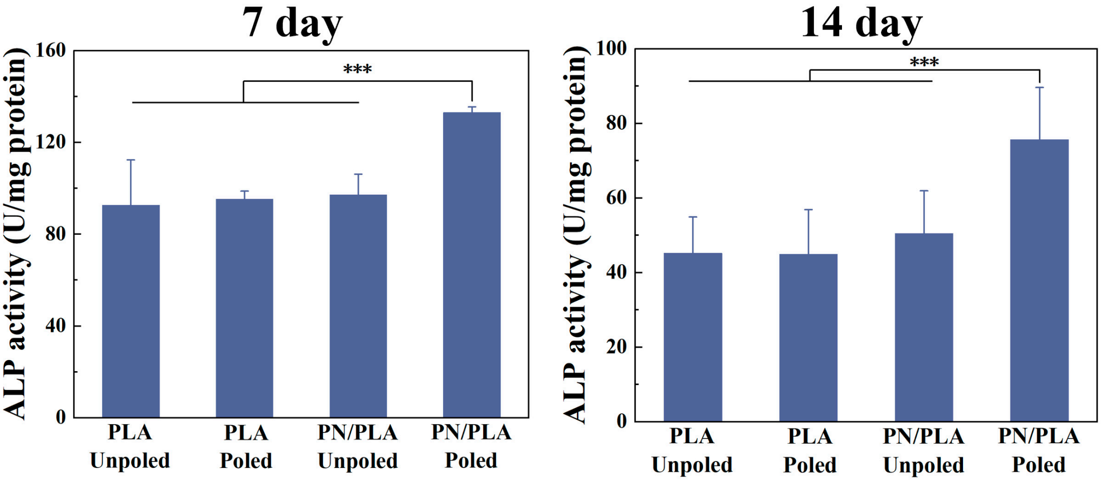

Figure 7. ALP activity of BMSCs seeded on PLA and PN/PLA (*** $p < 0.001$).

4. Conclusions

In this work, ferroelectric PVTF NPs were incorporated onto the degradable PLA surface to create PN/PLA membrane. PVTF NPs with ferroelectric β phase exhibited negative potentials after corona polarization. Therefore, it is speculated that PVTF NPs formed dispersed spots with negative potentials, thereby modulating the overall surface potential of PN/PLA membrane. Such negative surface potential promoted the adhesion, proliferation and early osteogenic differentiation of BMSCs. Meanwhile, PN/PLA showed degradability in simulated body fluid. The electroactivity and degradability could be joined together in this study, which is promising for tissue regeneration biomaterials, such as guided bone regeneration membrane.

Author Contributions: Methodology, S.S.; investigation, S.S. and X.X.; data curation, S.S., P.L. and X.H.; writing—original draft preparation, S.S. and S.F.; visualization, S.S. and X.X.; conceptualization, K.C. and S.S.; writing—review and editing, K.C. and C.W. All authors have read and agreed to the published version of the manuscript.

Funding: This research was funded by the National Natural Science Foundation of China (Grant No. 32271373, 52271252 and 52072339), National Funded Postdoctoral Program of China (GZC20232243) and Key Research and Development Program of Zhejiang Province(2021C03061).

Institutional Review Board Statement: Not applicable.

Informed Consent Statement: Not applicable.

Data Availability Statement: Data are contained within the article.

Conflicts of Interest: The authors declare no conflicts of interest.

References

1. Zhang, X.; Wang, T.; Zhang, Z.; Liu, H.; Li, L.; Wang, A.; Ouyang, J.; Xie, T.; Zhang, L.; Xue, J.; et al. Electrical stimulation system based on electroactive biomaterials for bone tissue engineering. *Mater. Today* **2023**, *68*, 177–203. [CrossRef]
2. Tandon, B.; Blaker, J.J.; Cartmell, S.H. Piezoelectric materials as stimulatory biomedical materials and scaffolds for bone repair. *Acta Biomater.* **2018**, *73*, 1–20. [CrossRef] [PubMed]

3. Levin, M.; Pezzulo, G.; Finkelstein, J.M. Endogenous Bioelectric Signaling Networks: Exploiting Voltage Gradients for Control of Growth and Form. *Annu. Rev. Biomed. Eng.* **2017**, *19*, 353–387. [CrossRef] [PubMed]
4. Das, K.K.; Basu, B.; Maiti, P.; Dubey, A.K. Piezoelectric nanogenerators for self-powered wearable and implantable bioelectronic devices. *Acta Biomater.* **2023**, *171*, 85–113. [CrossRef] [PubMed]
5. Marino, A.; Genchi, G.G.; Sinibaldi, E.; Ciofani, G. Piezoelectric Effects of Materials on Bio-Interfaces. *ACS Appl. Mater. Interfaces* **2017**, *9*, 17663–17680. [CrossRef]
6. Tandon, B.; Magaz, A.; Balint, R.; Blaker, J.J.; Cartmell, S.H. Electroactive biomaterials: Vehicles for controlled delivery of therapeutic agents for drug delivery and tissue regeneration. *Adv. Drug Deliv. Rev.* **2018**, *129*, 148–168. [CrossRef]
7. Tofail, S.A.M.; Bauer, J. Electrically Polarized Biomaterials. *Adv. Mater.* **2016**, *28*, 5470–5484. [CrossRef]
8. Qiao, Z.; Lian, M.; Liu, X.; Zhang, X.; Han, Y.; Ni, B.; Xu, R.; Yu, B.; Xu, Q.; Dai, K. Electreted Sandwich Membranes with Persistent Electrical Stimulation for Enhanced Bone Regeneration. *ACS Appl. Mater. Interfaces* **2022**, *14*, 31655–31666. [CrossRef]
9. Wu, C.; He, X.; Weng, W.; Zhang, T.; Huang, D.; Cheng, K.; Chen, Z. Electroactive extracellular Matrix/Polypyrrole composite films and their microenvironmental effects on osteogenic differentiation of BMSCs. *Chem. Eng. J.* **2022**, *443*, 136508. [CrossRef]
10. Fukada, E.; Yasuda, I. On the piezoelectric effect of bone. *J. Phys. Soc. Jpn.* **1957**, *12*, 1158–1162. [CrossRef]
11. Klee, D.; Ademovic, Z.; Bosserhoff, A.; Hoecker, H.; Maziolis, G.; Erli, H. Surface modification of poly(vinylidenefluoride) to improve the osteoblast adhesion. *Biomaterials* **2003**, *24*, 3663–3670. [CrossRef] [PubMed]
12. Shen, S.; He, X.; Chen, X.; Dong, L.; Cheng, K.; Weng, W. Enhanced osteogenic differentiation of mesenchymal stem cells on P(VDF-TrFE) layer coated microelectrodes. *J. Biomed. Mater. Res. Part B Appl. Biomater.* **2021**, *109*, 2227–2236. [CrossRef] [PubMed]
13. Andrew, J. Ferroelectric Polymers. *Science* **1983**, *220*, 4602.
14. Huang, Y.; Rui, G.; Li, Q.; Allahyarov, E.; Li, R.; Fukuto, M.; Zhong, G.; Xu, J.; Li, Z.; Taylor, P.L.; et al. Enhanced piezoelectricity from highly polarizable oriented amorphous fractions in biaxially oriented poly(vinylidene fluoride) with pure β crystals. *Nat. Commun.* **2021**, *12*, 675. [CrossRef] [PubMed]
15. Koga, K.; Nakano, N.; Hattori, T.; Ohigashi, H. Crystallization, field-induced phase transformation, thermally induced phase transition, and piezoelectric activity in P(vinylidene fluoride-TrFE) copolymers with high molar content of vinylidene fluoride. *J. Appl. Phys.* **1990**, *67*, 965–974. [CrossRef]
16. Tang, B.; Zhang, B.; Zhuang, J.; Wang, Q.; Dong, L.; Cheng, K.; Weng, W. Surface potential-governed cellular osteogenic differentiation on ferroelectric polyvinylidene fluoride trifluoroethylene films. *Acta Biomater.* **2018**, *74*, 291–301. [CrossRef] [PubMed]
17. Zhang, J.; He, X.; Chen, X.; Wu, Y.; Dong, L.; Cheng, K.; Lin, J.; Wang, H.; Weng, W. Enhancing osteogenic differentiation of BMSCs on high magnetoelectric response films. *Mater. Sci. Eng. C* **2020**, *113*, 110970. [CrossRef]
18. Zhang, J.; He, X.; Lin, S.; Chen, X.; Dong, L.; Lin, J.; Wang, H.; Weng, W.; Cheng, K. Accelerated Osteogenesis of Heterogeneous Electric Potential Gradient on CFO/P(VDF-TrFE) Membranes. *Adv. Mater. Interfaces* **2022**, *9*, 2102549. [CrossRef]
19. Liao, Y.; Wang, R.; Tian, M.; Qiu, C.; Fane, A.G. Fabrication of polyvinylidene fluoride (PVDF) nanofiber membranes by electro-spinning for direct contact membrane distillation. *J. Membr. Sci.* **2013**, *425–426*, 30–39. [CrossRef]
20. Bhatta, T.; Maharjan, P.; Cho, H.; Park, C.; Yoon, S.H.; Sharma, S.; Salauddin, M.; Rahman, M.T.; Rana, S.S.; Park, J.Y. High-performance triboelectric nanogenerator based on MXene functionalized polyvinylidene fluoride composite nanofibers. *Nano Energy* **2021**, *81*, 105670. [CrossRef]
21. Gao, S.; Sun, J.; Liu, P.; Zhang, F.; Zhang, W.; Yuan, S.; Li, J.; Jin, J. A Robust Polyionized Hydrogel with an Unprecedented Underwater Anti-Crude-Oil-Adhesion Property. *Adv. Mater.* **2016**, *28*, 5307–5314. [CrossRef]
22. Mishra, H.K.; Gupta, V.; Roy, K.; Babu, A.; Kumar, A.; Mandal, D. Revisiting of δ−PVDF nanoparticles via phase separation with giant piezoelectric response for the realization of self-powered biomedical sensors. *Nano Energy* **2022**, *95*, 107052. [CrossRef]
23. Fu, C.; Zhu, H.; Hoshino, N.; Akutagawa, T.; Mitsuishi, M. Interfacial Nanostructuring of Poly(vinylidene fluoride) Homopolymer with Predominant Ferroelectric Phases. *Langmuir* **2020**, *36*, 14083–14091. [CrossRef]
24. Das, R.; Le, T.T.; Schiff, B.; Chorsi, M.T.; Park, J.; Lam, P.; Kemerley, A.; Supran, A.M.; Eshed, A.; Luu, N.; et al. Biodegradable piezoelectric skin-wound scaffold. *Biomaterials* **2023**, *301*, 122270. [CrossRef] [PubMed]
25. Denning, D.; Kilpatrick, J.I.; Fukada, E.; Zhang, N.; Habelitz, S.; Fertala, A.; Gilchrist, M.D.; Zhang, Y.; Tofail, S.A.M.; Rodriguez, B.J. Piezoelectric Tensor of Collagen Fibrils Determined at the Nanoscale. *ACS Biomater. Sci. Eng.* **2017**, *3*, 929–935. [CrossRef] [PubMed]
26. Zhou, Z.; Qian, D.; Minary-Jolandan, M. Molecular Mechanism of Polarization and Piezoelectric Effect in Super-Twisted Collagen. *ACS Biomater. Sci. Eng.* **2016**, *2*, 929–936. [CrossRef] [PubMed]
27. Seyedhosseini, E.; Romanyuk, K.; Vasileva, D.; Vasilev, S.; Nuraeva, A.; Zelenovskiy, P.; Ivanov, M.; Morozovska, A.N.; Shur, V.Y.; Lu, H.; et al. Self-Assembly of Organic Ferroelectrics by Evaporative Dewetting: A Case of β-Glycine. *ACS Appl. Mater. Interfaces* **2017**, *9*, 20029–20037. [CrossRef] [PubMed]
28. Hosseini, E.S.; Manjakkal, L.; Shakthivel, D.; Dahiya, R. Glycine–Chitosan-Based Flexible Biodegradable Piezoelectric Pressure Sensor. *ACS Appl. Mater. Interfaces* **2020**, *12*, 9008–9016. [CrossRef]
29. Madhavan Nampoothiri, K.; Nair, N.R.; John, R.P. An overview of the recent developments in polylactide (PLA) research. *Bioresour. Technol.* **2010**, *101*, 8493–8501. [CrossRef]
30. Curry, E.J.; Ke, K.; Chorsi, M.T.; Wrobel, K.S.; Miller, A.N.; Patel, A.; Kim, I.; Feng, J.; Yue, L.; Wu, Q.; et al. Biodegradable Piezoelectric Force Sensor. *Proc. Natl. Acad. Sci. USA* **2018**, *115*, 909–914. [CrossRef]

31. Masamichi, A.; Hideki, K.; Keisuke, K.; Yoshiro, T. Film Sensor Device Fabricated by a Piezoelectric Poly(L-lactic acid) Film. *Jpn. J. Appl. Phys.* **2012**, *51*, 09LD14.
32. Sawano, M.; Tahara, K.; Orita, Y.; Nakayama, M.; Tajitsu, Y. New design of actuator using shear piezoelectricity of a chiral polymer, and prototype device. *Polym. Int.* **2010**, *59*, 365–370. [CrossRef]
33. Lee, S.J.; Arun, A.P.; Kim, K.J. Piezoelectric properties of electrospun poly(l-lactic acid) nanofiber web. *Mater. Lett.* **2015**, *148*, 58–62. [CrossRef]
34. Smith, M.; Calahorra, Y.; Jing, Q.; Kar-Narayan, S. Direct observation of shear piezoelectricity in poly-l-lactic acid nanowires. *APL Mater.* **2017**, *5*, 074105. [CrossRef]
35. Xiao, Z.; Dong, Q.; Sharma, P.; Yuan, Y.; Mao, B.; Tian, W.; Gruverman, A.; Huang, J. Synthesis and Application of Ferroelectric P(VDF-TrFE) Nanoparticles in Organic Photovoltaic Devices for High Efficiency. *Adv. Energy Mater.* **2013**, *3*, 1581–1588. [CrossRef]
36. Todd, P.S. The Real Reason Why Oil and Water Don't Mix. *J. Chem. Educ.* **1998**, *75*, 116.
37. Rotan, M.; Zhuk, M.; Glaum, J. Activation of ferroelectric implant ceramics by corona discharge poling. *J. Eur. Ceram. Soc.* **2020**, *40*, 5402–5409. [CrossRef]
38. Mahadeva, S.K.; Berring, J.; Walus, K.; Stoeber, B. Effect of poling time and grid voltage on phase transition and piezoelectricity of poly(vinyledene fluoride) thin films using corona poling. *J. Phys. D Appl. Phys.* **2013**, *46*, 285301–285305. [CrossRef]
39. Meng, N.; Zhu, X.; Mao, R.; Reece, M.J.; Bilotti, E. Nanoscale interfacial electroactivity in PVDF/PVDF-TrFE blended films with enhanced dielectric and ferroelectric properties. *J. Mater. Chem. C* **2017**, *5*, 3296–3305. [CrossRef]
40. Singh, H.H.; Khare, N. KPFM Study of Flexible Ferroelectric Polymer/Water Interface for Understanding the Working Principle of Liquid–Solid Triboelectric Nanogenerator. *Adv. Mater. Interfaces* **2021**, *8*, 2100032. [CrossRef]
41. Ruiz, A.; Seoane, N.; Claramunt, S.; García-Loureiro, A.; Porti, M.; Couso, C.; Martin-Martinez, J.; Nafria, M. Workfunction fluctuations in polycrystalline TiN observed with KPFM and their impact on MOSFETs variability. *Appl. Phys. Lett.* **2019**, *114*, 093502. [CrossRef]
42. Barroca, N.; Marote, A.; Vieira, S.I.; Almeida, A.; Fernandes, M.H.V.; Vilarinho, P.M.; Da Cruz E Silva, O.A.B. Electrically polarized PLLA nanofibers as neural tissue engineering scaffolds with improved neuritogenesis. *Colloids Surf. B Biointerfaces* **2018**, *167*, 93–103. [CrossRef] [PubMed]
43. Grizzi, I.; Garreau, H.; Li, S.; Vert, M. Hydrolytic degradation of devices based on poly[m-lactic acid) size- dependence. *Biomaterials* **1995**, *16*, 305–311. [CrossRef]
44. Li, S.; McCarthy, S. Influence of Crystallinity and Stereochemistry on the Enzymatic Degradation of Poly(lactide)s. *Macromolecules* **1999**, *32*, 4454–4456. [CrossRef]
45. Zhou, Q.; Xanthos, M. Nanoclay and crystallinity effects on the hydrolytic degradation of polylactides. *Polym. Degrad. Stab.* **2008**, *93*, 1450–1459. [CrossRef]